

1 A direct comparison between field-measured

2 and sensor-based estimates of soil carbon

3 dioxide flux across six National Ecological

4 Observatory Network sites enabled by the

5 neonSoilFlux R package

6 John Zobitz¹ Ed Ayres² Zoey Werbin³ Ridwan Abdi¹

7 Natalie Ashburner-Wright⁴ Lillian Brown⁴

8 Ryan Frink-Sobierajski⁴ Lajntxiag Lee¹ Dijonë Mehmeti¹

9 Christina Tran⁴ Ly Xiong¹ Naupaka Zimmerman⁴

10 ¹ Augsburg University, 2211 Riverside Avenue, Minneapolis, MN 55454

11 ² National Ecological Observatory Network, 1685 38th Street, Suite 100, Boulder, CO 80301

12 ³ Boston University, 5 Cummington Street, Boston, MA 02215

13 ⁴ University of San Francisco, 2130 Fulton Street, San Francisco, CA 94117

¹⁴ **Acknowledgments**

¹⁵ JZ acknowledges Kathleen O'Rourke for code development. NZ thanks technical staff at
¹⁶ USF for support with field gear assembly and shipping. We thank the NEON field staff
¹⁷ and assignable assets teams for facilitating each of the six NEON site visits. We are grateful
¹⁸ to LI-COR technical staff for helpful discussions about optimal sampling methods. This work
¹⁹ was supported by NSF DEB grant #2017829 awarded to JZ, and NSF DEB grant #2017860
²⁰ awarded to NZ.

²¹ **Conflict of Interest Statements**

²² None of the authors have a financial, personal, or professional conflict of interest related to
²³ this work.

²⁴ **Author Contributions**

²⁵ Conceptualization: JZ, NZ; Methodology: EA, JZ, NZ; Software: JZ, NZ, ZW, E A, DM, RA,
²⁶ LX, LL; Validation: JZ, NZ; Formal Analysis: JZ, NZ, DM, RA, LX, LL; Investigation: JZ,
²⁷ NZ, RF-S, CT, NA-W, LB; Resources: JZ, NZ; Data curation: JZ, NZ, DM, LX; Writing
²⁸ – original draft: JZ, NZ; Writing – review and editing: JZ, NZ, ZW, EA, CT, DM, LX,;
²⁹ Visualization: JZ, NZ, DM, RA, LX; Supervision: JZ; NZ; Project Administration: JZ; NZ;
³⁰ Funding Acquisition: JZ; NZ

³¹ **Data Availability**

³² Data available from the Zenodo LINK <http://dx.doi.org/10.5061/dryad.41qh7> (Kiere & Drummond 2016)."

³⁴ **1 Abstract**

³⁵ A key component of constraining the uncertainty of the terrestrial carbon sink is quantification
³⁶ of terrestrial soil carbon fluxes, which vary across time and ecosystem type. One method for
³⁷ the estimation of these fluxes and their associated uncertainties is the flux gradient method,
³⁸ which can be calculated via a variety of existing approaches. Robust estimation of soil carbon
³⁹ fluxes on a sub-daily level requires measurements of soil CO₂ concentration, water content,
⁴⁰ temperature, and other environmental measurements and soil properties. These data are
⁴¹ publicly available from the National Ecological Observatory Network at sites spanning a range
⁴² of 20 different ecoclimatic domains across the continental United States, Puerto Rico, Alaska,
⁴³ and Hawai'i. We present an R software package (`neonSoilFlux`) that acquires NEON soil
⁴⁴ environmental data and computes soil carbon flux at a half-hourly time step at a user-specified
⁴⁵ NEON site and month in a tidy data format. To validate the computed fluxes, we visited six
⁴⁶ focal NEON sites and measured soil carbon fluxes using a closed-dynamic chamber approach.
⁴⁷ The validation confirmed that a primary challenge in reducing soil carbon flux uncertainty is
⁴⁸ correctly characterizing diffusivity and soil water content across the soil profile. Outputs from
⁴⁹ the `neonSoilFlux` package contribute to existing databases of soil carbon flux measurements,
⁵⁰ providing near real-time estimates of a critical component of the terrestrial carbon cycle.

⁵¹ **1.1 Keywords**

⁵² Soil carbon, carbon dioxide, flux gradient, carbon cycle, field validation, soil respiration, ecosys-
⁵³ tem variability, diffusion

⁵⁴ **2 Data for peer review**

⁵⁵ Anonymous data and code for peer review is available here: [LINK](#)

⁵⁶ **3 Introduction**

⁵⁷ Soils contain the largest reservoir of terrestrial carbon (Jobbágy & Jackson, 2000). A critical
⁵⁸ component of this reservoir is soil organic matter, the accumulation of which is influenced
⁵⁹ by biotic factors such as above-ground plant inputs (Jackson et al., 2017). These inputs in
⁶⁰ turn are influenced by environmental factors such as growing season length, temperature, and
⁶¹ moisture (Desai et al., 2022), which also affect the breakdown of soil organic matter and its
⁶² return to the atmosphere. Across heterogeneous terrestrial landscapes, the interplay between
⁶³ these biotic and abiotic factors influence the size of the soil contribution to the terrestrial
⁶⁴ carbon sink (Friedlingstein et al., 2023). However, the heterogeneity of these processes across
⁶⁵ diverse ecosystems in the context of rapid environmental change leads to large uncertainty in
⁶⁶ the magnitude of this sink in the future, and thus a pressing need to quantify changes in soil
⁶⁷ carbon pools and fluxes across scales.

⁶⁸ Ecological observation networks such as the United States' National Ecological Observatory
⁶⁹ Network (NEON) and others (e.g. FLUXNET or the Integrated Carbon Observation System)
⁷⁰ present a significant advancement in the nearly continuous observation of biogeochemical pro-
⁷¹ cesses at the continental scale. Notably, at 47 terrestrial sites across the continental United
⁷² States, NEON provides half-hourly measurements of soil CO₂ concentration, temperature,
⁷³ and moisture at different vertical depths. Each of these NEON sites also encompasses mea-
⁷⁴ surements of the cumulative sum of all ecosystem carbon fluxes in an airshed using the eddy
⁷⁵ covariance technique (Balderuppi, 2014). Soil observations provided by NEON are on the same

76 timescale and standardized with eddy covariance measurements from FLUXNET. These types
77 of nearly continuous observational data (NEON and FLUXNET) can be used to reconcile dif-
78 ferences between model-derived or data-estimated components of ecosystem carbon flux (Jian
79 et al., 2022; Luo et al., 2011; Phillips et al., 2017; J. Shao et al., 2015; P. Shao et al., 2013;
80 Sihi et al., 2016).

81 Estimated or observed soil carbon fluxes are a key metric for understanding change in soil
82 carbon pools over time (Bond-Lamberty et al., 2024). A soil carbon flux to the atmosphere
83 (F_S , units $\mu\text{mol m}^{-2} \text{s}^{-1}$), represents the aggregate process of transfer of soil CO_2 to the
84 atmosphere from physical and biological processes (e.g. diffusion and respiration). Soil carbon
85 fluxes can be assumed to encompass soil carbon respiration from autotrophic or heterotrophic
86 sources (Davidson et al., 2006), typically assumed to be static across the soil biome and
87 modeled with a exponential Q_{10} paradigm (Bond-Lamberty et al., 2004; Chen & Tian, 2005;
88 Hamdi et al., 2013).

89 One method by which F_S is measured in the field is through the use of soil chambers in a closed,
90 well-mixed system (Norman et al., 1997) with headspace trace gas concentrations measured
91 with an infrared gas analyzer (IRGA). F_S can also be estimated from soil CO_2 measurements
92 at different depths in the soil using the flux-gradient method (Maier & Schack-Kirchner, 2014).
93 This method is an approach that uses conservation of mass to calculate flux at a vertical soil
94 depth z at steady state by applying Fick's law of diffusion. A simplifying assumption for the
95 flux-gradient method is that there is no mass transfer in the other spatial dimensions x and y
96 (Maier & Schack-Kirchner, 2014). The diffusivity profile, a key component of this calculation,
97 varies across the soil depth as a function of soil temperature, soil volumetric water content,
98 atmospheric air pressure, and soil bulk density (Millington & Shearer, 1971; Moldrup et al.,
99 1999; Sallam et al., 1984).

100 Databases such as the Soil Respiration Database (SRDB) or the Continuous Soil Respiration

101 Database (COSORE) add to the growing network of resources for making collected observa-
102 tions of soil fluxes available to other workers (Bond-Lamberty, 2018; Bond-Lamberty et al.,
103 2020; Bond-Lamberty & Thomson, 2010; Jian et al., 2021; Jiang et al., 2024). However, these
104 databases currently encompass primarily direct soil measurements of fluxes (i.e. those using
105 methods like the closed-chamber method described above). Currently, NEON provides all
106 measurements to calculate F_S from Fick's law, but soil flux as a derived data product was
107 descoped from the initial network launch due to budget constraints (Berenbaum et al., 2015).
108 Deriving estimates of F_S using continuous sensor data across NEON sites thus represents a
109 high priority.

110 This study describes an R software package, `neonSoilFlux`, that can be used to derive a
111 standardized estimate of F_S at all terrestrial NEON sites. After calculating these flux estimates,
112 we then validated them against direct chamber-based field observations of soil carbon dioxide
113 flux from a subset of terrestrial NEON sites spanning six states.

114 Key objectives of this study are to:

- 115 1. Apply the flux-gradient method to estimate soil CO₂ flux from continuous sensor mea-
116 surements across NEON sites.
- 117 2. Benchmark estimated soil carbon fluxes against field measurements (e.g. direct chamber
118 measurements of soil flux).
- 119 3. Identify sources of error in the flux-gradient approach across diverse sites in order to
120 guide future work.

₁₂₁ **4 Materials and Methods**

₁₂₂ **4.1 Field methods**

₁₂₃ **4.1.1 Focal NEON Sites**

₁₂₄ In order to acquire field data to validate model predictions of flux, we selected six terrestrial
₁₂₅ NEON sites for analysis. We conducted field measurement campaigns at these sites, which
₁₂₆ span a range of environmental gradients and terrestrial domains (Table 1). SJER, SRER, and
₁₂₇ WREF were visited during May and June of 2022, and WOOD, KONZ, and UNDE during
₁₂₈ May and June of 2024.

₁₂₉ Over the course of two field campaigns in 2022 and 2024, we conducted week-long visits at
₁₃₀ each site. In consultation with NEON field staff, we first selected a specific plot in the soil
₁₃₁ sampling array to maximize the concurrent availability of sensor data.

₁₃₂ **4.1.2 Soil collar placement**

₁₃₃ Either one (2022 sampling campaign) or two (2024 sampling campaign) PVC soil collars (20.1
₁₃₄ cm inside diameter) were installed in close proximity to the permanent NEON soil sensors at
₁₃₅ each site (Figure 1). The soil plot where measurements were taken was chosen at each site
₁₃₆ in consultation with NEON staff to maximize likelihood of quality soil sensor measurements
₁₃₇ during the duration of the IRGA measurements at each site. After installation, collar(s) were
₁₃₈ left to equilibrate for approximately 24 hours prior to measurements being taken.

¹³⁹ **4.1.3 Infrared gas analyzer measurements of soil CO₂ flux**

¹⁴⁰ In 2022, we then made measurements of flux on an hourly interval for 8 hours each day.
¹⁴¹ Measurements were taken from roughly 8 am to 4 pm, with the time interval selected to
¹⁴² capture the majority of the diurnal gradient of soil temperature each day. These measurements
¹⁴³ were made using a LI-6800 infrared gas analyzer instrument (LI-COR Environmental, Lincoln,
¹⁴⁴ NE) fitted with a soil chamber attachment (attachment 6800-09). In 2024, we again used
¹⁴⁵ the same LI-6800 instrument, but made half-hourly measurements over an approximately 8
¹⁴⁶ hour period. In addition, we also installed a second collar and used a second instrument, an
¹⁴⁷ LI-870 CO₂ IRGA, connected to an automated robotic chamber (LI-COR chamber 8200-104)
¹⁴⁸ controlled by an LI-8250 multiplexer, to make automated measurements. The multiplexer was
¹⁴⁹ configured to take half-hourly measurements 24 hours a day for the duration of our sampling
¹⁵⁰ bout at each site. Each instrument was paired with a soil temperature and moisture probe
¹⁵¹ (Stevens HydraProbe, Stevens Water, Portland, OR) that was used to make soil temperature
¹⁵² and moisture measurements concurrent with the CO₂ flux measurements. Chamber volumes
¹⁵³ were set by measuring collar offsets at each site. System checks were conducted daily for the
¹⁵⁴ LI-6800 and weekly for the LI-8250. Instruments were factory calibrated before each field
¹⁵⁵ season.

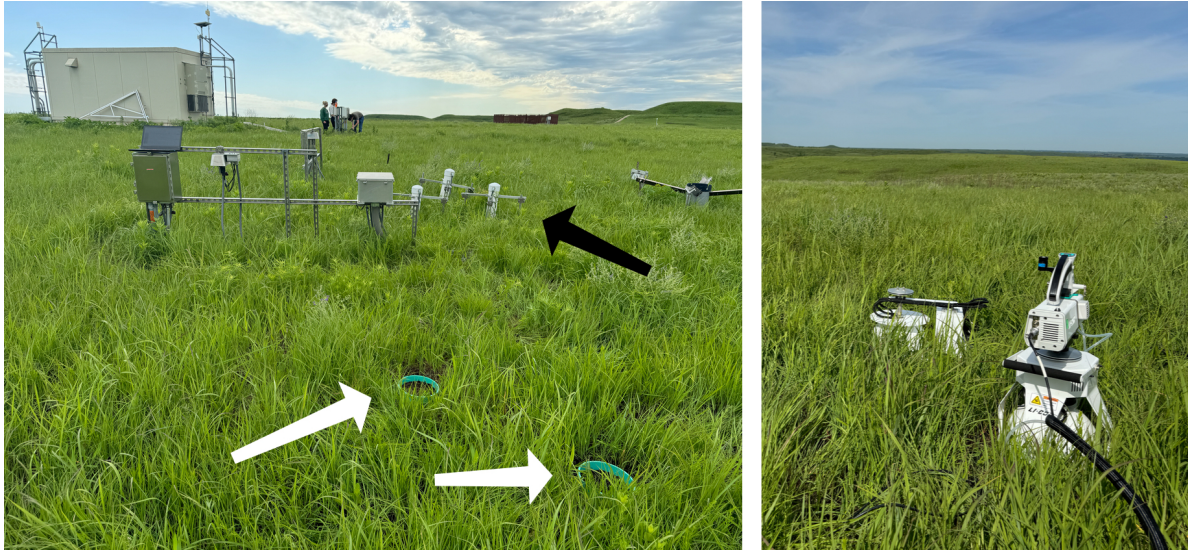


Figure 1: Spatial layout of field sampling using a closed-dynamic chamber setup at a representative NEON site (KONZ). Left image shows collars (white arrows) and permanent soil sensor installation (black arrow) and right image shows the LI-6800 (foreground) and LI-8200-104 (background) instruments placed on the collars.

Table 1: Listing of NEON sites studied for field work and analysis. $\overline{T_S}$: average soil temperature during field measurements. \overline{SWC} : average soil water content during field measurements. Soil plot refers to the particular location in the soil sensor array (denoted as HOR by NEON) where field measurements were made.

Site (NEON site ID)	Location	Ecosystem type	Mean annual tempera- ture	$\overline{T_S}$ (°)	Mean annual precipita- tion	\overline{SWC} (%)	Field measure- ment dates	Soil plot
Santa	31.91068,	Shrubland	19.3°C	47.6°	346 mm	4.0%	29 May	004
Rita	-						2024 - 01	
Experi- mental Range (SRER)	110.83549						June 2024	

Table 1: Listing of NEON sites studied for field work and analysis. \bar{T}_S : average soil temperature during field measurements. \bar{SWC} : average soil water content during field measurements. Soil plot refers to the particular location in the soil sensor array (denoted as HOR by NEON) where field measurements were made.

Site (NEON site ID)	Location	Ecosystem type	Mean annual tempera- ture	\bar{T}_S (°)	Mean annual precipita- tion	\bar{SWC} (%)	Field measure- ment dates	Soil plot
San Joaquin Experimental Range (SJER)	37.10878, -	Oak woodland	16.4°C	41.7°	540 mm	1.2%	01 June 2022 - 04	005
Wind River Experimental Forest (WREF)	45.82049, -	Evergreen forest	9.2°C	15.3°	2225 mm	27.2%	07 June 2022	001
Chase Lake National Wildlife Refuge (WOOD)	121.95191	Restored prairie	4.9°C	14.9°	495 mm	14.9%	03 June 2024 - 09	001
Konza Prairie Biological Station (KONZ)	47.1282, -	Tallgrass prairie	12.4°C	23.4°	870 mm	23.4%	29 May 2024 - 01	001
	99.241334	grassland					June 2024	
	96.563075						June 2024	

Table 1: Listing of NEON sites studied for field work and analysis. \bar{T}_S : average soil temperature during field measurements. \bar{SWC} : average soil water content during field measurements. Soil plot refers to the particular location in the soil sensor array (denoted as HOR by NEON) where field measurements were made.

Site (NEON site ID)	Location	Ecosystem type	Mean annual tempera- ture	\bar{T}_S (°)	Mean annual precipita- tion	\bar{SWC} (%)	Field measure- ment dates	Soil plot
University of Notre Dame Environmental Research Center (UNDE)	46.23391, - 89.537254	Deciduous forest	4.3°	13.0°	802 mm	13.0%	22 May 2024 - 25 May 2024	004

156 4.1.4 Post-collection processing of data

157 We used LI-COR SoilFluxPro software (v 5.3.1) to assess the data after collection and to inform
 158 sampling parameters. We checked appropriateness of dead band and measurement durations
 159 using built-in evaluation tools. Based on this, the deadband period was set for 30-40 seconds,
 160 depending on the site, and the measurement duration was 180 seconds with a 30 second pre-
 161 purge and a 30 second post-purge. We also assessed the R^2 of linear and exponential model
 162 fits to measured CO_2 to verify measurement quality.

163 4.2 neonSoilFlux R package

164 We developed an R package (`neonSoilFlux`; <https://CRAN.R-project.org/package=neonSoilFlux>)
 165 to compute half-hourly soil carbon fluxes and uncertainties from NEON data. The

166 objective of the `neonSoilFlux` package is a unified workflow for soil data acquisition
167 and analysis that supplements the existing data acquisition R package `neonUtilities`
168 (<https://CRAN.R-project.org/package=neonUtilities>). Figure 2 outlines the basic workflow
169 of the package.

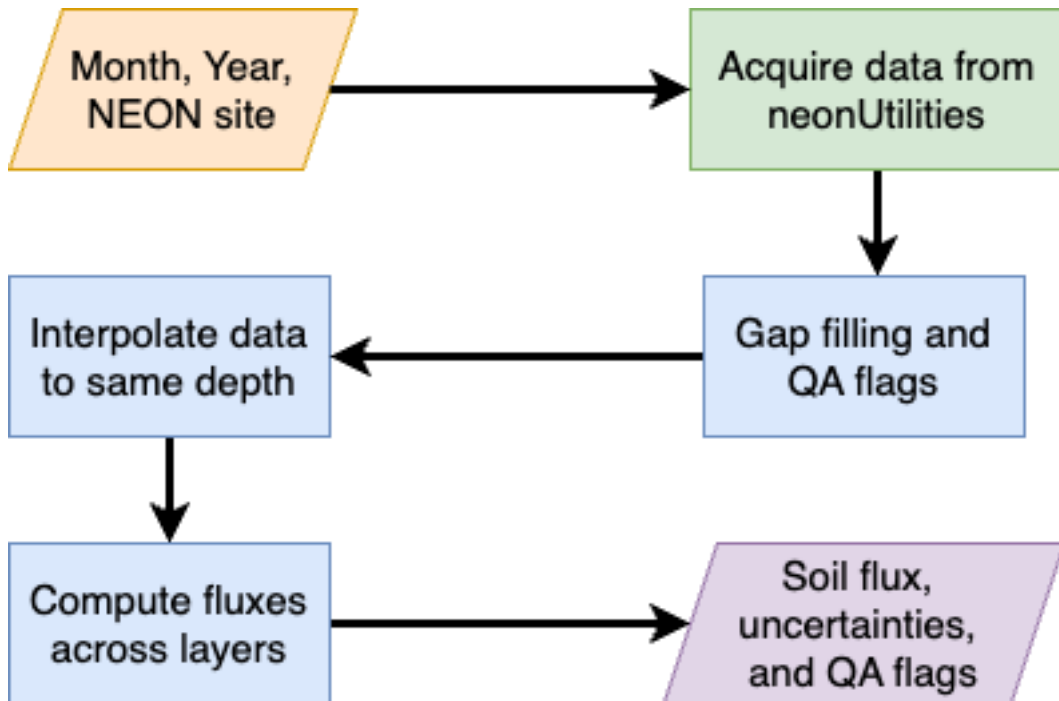


Figure 2: Diagram of `neonSoilFlux` R package. For a given month, year and NEON site (orange parallelogram), the package acquires all relevant data to compute F_S using the `neonUtilities` R package (green rectangle). Data are gap-filled according to reported QA flags and interpolated to the same measurement depth before computing the soil flux, uncertainties, and final QA flags (blue rectangles). The package reports the associated soil flux, uncertainties, and quality assurance (QA) flags for the user (purple parallelogram).

170 At a given NEON observation there are five replicate soil plots, each with measurements of
171 soil CO₂ concentration, soil temperature, and soil moisture at different depths (Figure 3). The
172 `neonSoilFlux` package acquires measured soil water content (National Ecological Observatory
173 Network (NEON), 2024e), soil CO₂ concentration (National Ecological Observatory Network
174 (NEON), 2024b), barometric pressure from the nearby tower (National Ecological Observa-

tory Network (NEON), 2024a), soil temperature (National Ecological Observatory Network (NEON), 2024d), and soil properties (e.g. bulk density) (National Ecological Observatory Network (NEON), 2024c). The static soil properties were collected from a nearby soil pit during site characterization and are assumed to be constant at each site.

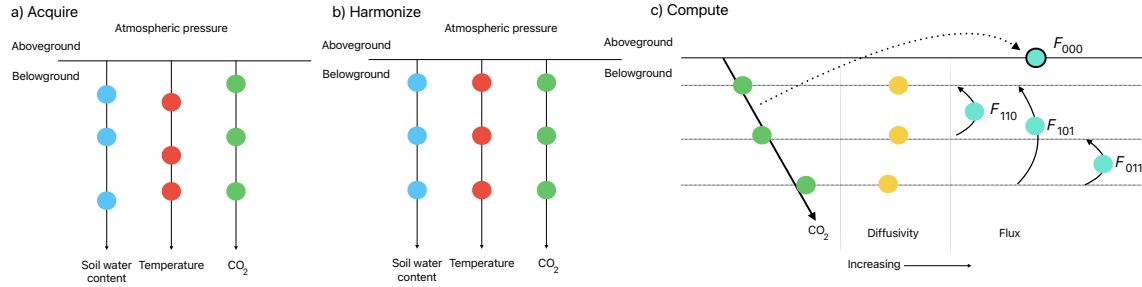


Figure 3: Model diagram for data workflow for the `neonSoilFlux` R package. a) Acquire: Data are obtained from given NEON location and horizontal sensor location, which includes soil water content, soil temperature, CO_2 concentration, and atmospheric pressure. All data are screened for quality assurance, with gap-filling of missing data reported. b) Any belowground data are then harmonized to the same depth as CO_2 concentrations using linear regression. c) The flux across a given depth is computed via Fick's law, denoted with F_{ijk} , where i , j , or k are either 0 or 1 denoting the layers the flux is computed across (i = closest to surface, k = deepest). F_{000} represents a flux estimate where the gradient dC/dz is the slope of a linear regression of CO_2 with depth.

The workflow to computing a value of F_S with the `neonSoilFlux` consists of three primary steps, illustrate in Figure 3. First, NEON data are acquired for a given site and month via the `neonUtilities` R package (yellow parallelogram and green rectangle in Figure 2 and Panel a in Figure 3). Acquired environmental data can be exported to a comma separated value file for additional analysis. Quality assurance (QA) flags with an observation are reported as an indicator variable.

The next step is harmonizing the data to compute soil fluxes across soil layers. This step consists of three different actions (blue rectangles in Figure 2 and Panel b in Figure 3). If a given observation by NEON is reported as not passing a quality assurance check, we applied

188 a gap filling method to replace that measurement with its monthly mean at that same depth
189 (Section 4.2.1). Belowground measurements of soil water and soil temperature are then inter-
190 polated to the same depth as soil CO₂ measurements. The diffusivity (Section 4.2.2) and soil
191 flux across different soil layers (Section 4.2.3) are then computed.

192 The final step is computing a surface soil flux through extrapolation to the surface (purple
193 parallelogram in Figure 2 and Panel c in Figure 3). Uncertainty on a soil flux measurement is
194 computed through quadrature. An aggregate quality assurance (QA) flag for each environmen-
195 tal measurement is also reported, representing if any gap-filled measurements were used in the
196 computation of a soil flux. Within the soil flux-gradient method, several different approaches
197 can be used to derive a surface flux (Maier & Schack-Kirchner, 2014); the `neonSoilFlux`
198 package reports four different possible values of soil surface flux (Section 4.2.3).

199 4.2.1 Gap-filling routine

200 NEON reports QA flags as a binary value for a given measurement and half-hourly time. We
201 replaced any flagged measurements at a location's spatial depth z with a bootstrapped sample
202 of the monthly mean for all un-flagged measurements for that month. These measurements are
203 represented by the vector \mathbf{m} , standard errors σ , and the 95% confidence interval (the so-called
204 expanded uncertainty, Farrance & Frenkel (2012)) ϵ . All of these vectors have length M . We
205 have that $\vec{\sigma}_i \leq \vec{\epsilon}_i$. We define the bias as $\mathbf{b} = \sqrt{\epsilon^2 - \sigma^2}$.

206 We generate a vector of bootstrap samples of the distribution of the monthly mean \bar{m} and
207 monthly standard error $\bar{\sigma}$ the following ways:

- 208 1. Randomly sample from the uncertainty and bias independently: σ_j and the bias \mathbf{b}_k (not
209 necessarily the same sample).

- 210 2. Generate a vector \mathbf{n} of length N , where \mathbf{n}_i is a random sample from a normal distribution
 211 with mean m_i and standard deviation σ_j . Since $M < N$, values from \mathbf{m} will be reused.
 212 3. With these N random samples, $\bar{y}_i = \vec{x} + \vec{b}_k$ and s_i is the sample standard deviation of \vec{x} .
 213 We expect that $s_i \approx \vec{\sigma}_j$.
 214 4. The reported monthly mean and standard deviation are then computed $\bar{\bar{y}}$ and \bar{s} . Mea-
 215 surements and uncertainties that did not pass the QA check are then substituted with
 216 $\bar{\bar{y}}$ and \bar{s} .

217 This gap-filling method described here provides a consistent approach for each data stream,
 218 however we recognize that other gap-filling alternatives may be warranted for longer-term gaps
 219 (e.g. such as correlations with other NEON measurement levels and soil plots), or measure-
 220 ment specific gap-filling routines. We discuss the effect of gap-filling on our measurements in
 221 Section 6.

222 **4.2.2 Soil diffusivity**

223 Soil diffusivity D_a at a given measurement depth is the product of the diffusivity in free air
 224 $D_{a,0}$ ($\text{m}^2 \text{ s}^{-1}$) and the tortuosity ξ (no units) (Millington & Shearer, 1971).

225 We compute $D_{a,0}$ with Equation 1:

$$D_{a,0} = 0.0000147 \cdot \left(\frac{T_i + 273.15}{293.15} \right)^{1.75} \cdot \left(\frac{P}{101.3} \right) \quad (1)$$

226 where T_i is soil temperature ($^\circ\text{C}$) at depth i (National Ecological Observatory Network
 227 (NEON), 2024d) and P surface barometric pressure (kPa) (National Ecological Observatory
 228 Network (NEON), 2024a).

229 Previous studies by Sallam et al. (1984) and Tang et al. (2003) demonstrated the sensitivity
 230 of modeled F_S depending on the tortuosity model used to compute diffusivity. At low soil
 231 water content, the choice of tortuosity model may lead to order of magnitude differences in
 232 D_a , which in turn affect modeled F_S . The `neonSoilFlux` package uses two different models
 233 for ξ , representing the extremes reported in Sallam et al. (1984). The first approach uses the
 234 Millington-Quirk model for diffusivity, Equation 2 (Millington & Shearer, 1971):

$$\xi = \frac{(\phi - SWC_i)^{10/3}}{\phi^2} \quad (2)$$

235 In Equation 2, SWC is the soil water content at depth i (National Ecological Observatory
 236 Network (NEON), 2024e) and ϕ is the porosity (Equation 3), which in turn is a function of
 237 soil physical properties (National Ecological Observatory Network (NEON), 2024c):

$$\phi = \left(1 - \frac{\rho_s}{\rho_m}\right) (1 - f_V) \quad (3)$$

238 In Equation 3, ρ_m is the particle density of mineral soil (2.65 g cm^{-3}), ρ_s the soil bulk density
 239 (g cm^{-3}) excluding coarse fragments greater than 2 mm (National Ecological Observatory
 240 Network (NEON), 2024c). The term f_V is a site-specific value that accounts for the proportion
 241 of soil fragments between 2-20 mm. Soil fragments greater than 20 mm were not estimated
 242 due to limitations in the amount of soil that can be analyzed (National Ecological Observatory
 243 Network (NEON), 2024c). We assume there are no pores within rocks.

244 The second approach to calculate ξ is the Marshall model (Marshall, 1959), where $\xi = \phi^{1.5}$,
 245 with ϕ defined from Equation 3.

246 **4.2.3 Soil flux computation**

247 We applied Fick's law (Equation 4) to compute the soil flux F_{ij} ($\mu\text{mol m}^{-2} \text{s}^{-1}$) across two
248 soil depths i and j :

$$F_{ij} = -D_a \frac{dC}{dz} \quad (4)$$

249 where D_a is the diffusivity ($\text{m}^2 \text{s}^{-1}$) and $\frac{dC}{dz}$ is the gradient of CO_2 molar concentration
250 ($\mu\text{mol m}^{-3}$, so the gradient has units of $\mu\text{mol m}^{-3} \text{m}^{-1}$). The soil surface flux is theoretically
251 defined by applying Equation 4 to measurements collected at the soil surface and directly
252 below the surface. Measurements of soil temperature, soil water content, and soil CO_2 molar
253 concentration across the soil profile allow for application of Equation 4 across different soil
254 depths. Each site had three measurement layers, so we denote the flux between which two
255 layers as a three-digit subscript F_{ijk} with indicator variables i , j , and k indicate if a given
256 layer was used (written in order of increasing depth), according to the following:

- 257 • F_{000} is a surface flux estimate using the intercept of the linear regression of D_a with
258 depth and the slope from the linear regression of CO_2 with depth (which represents $\frac{dC}{dz}$
259 in Fick's Law). Tang et al. (2003) used this approach to compute fluxes in an oak-grass
260 savannah.
- 261 • F_{110} , F_{011} are fluxes across the two most shallow layers and two deepest layers respec-
262 tively. The diffusivity used in Fick's Law is always at the deeper measurement layer.
263 When used as a surface flux estimate we assume CO_2 remains constant above this flux
264 depth.
- 265 • F_{101} is a surface flux estimate using linear extrapolation using concentration measure-
266 ments between the shallowest and deepest measurement layer. Hirano et al. (2003) and

267 Tang et al. (2005) used an approach similar to F_{101} in a temperate deciduous broadleaf
268 forest and ponderosa pine forest respectively.

269 Uncertainty in all F_{ijk} is computed through quadrature (Taylor, 2022).

270 **4.3 Post processing evaluation**

271 Following collection of field measurements from the LICOR and calculation of the soil fluxes
272 from `neonSoilFlux` package, we compared measured F_S (from the LICOR instruments) to a
273 given soil flux calculation `neonSoilFlux` for each site and flux computation method. Statistics
274 included the associated R^2 value, root mean squared error (RMSE), and signal to noise ratio
275 (SNR), defined as the ratio of a modeled soil flux (F_{ijk}) from `neonSoilFlux` to its quadrature
276 uncertainty (σ_{ijk}).

277 We observed that the range of values (e.g. $F_{ijk} \pm \sigma_{ijk}$) was much larger than the measured
278 field flux. We evaluated $|F_S - F_{ijk}| < (1 - \epsilon)\sigma_{ijk}$, where F_S is a measured field soil flux
279 from the LICOR 6800 (the LICOR 8250 was used at only three sites). The parameter ϵ was
280 an uncertainty reduction factor to evaluate how much the quadrature uncertainty could be
281 reduced while maintaining precision between modeled F_{ijk} and measured F_S .

282 Finally, for a half-hourly interval we also computed a *post hoc* D_a using the LICOR flux along
283 with the CO_2 surface gradient reported by NEON using the measurement levels closest to the
284 surface.

285 **5 Results**

286 Figure 4 reports the timeseries of out the measured fluxes from the LICOR 6800 and 8250 com-
 287 pared to modeled soil fluxes from the `neonSoilFlux` R package. Figure 5 and and computed
 288 fluxes and uncertainty at each measurement site. Results are reported in local time. Positive
 289 values of the flux indicate that there is a flux moving towards the surface. For ease of clarity
 290 the fluxes at F_{111} and F_{000} are only shown in the top row (surface), followed by the fluxes at
 291 individual separate layer (F_{100} , F_{010} , F_{001}). Overall, with the exception of WREF and SRER
 292 (discussed later) the computed fluxes were on the same order of magnitude and timing as the
 293 measured field fluxes.

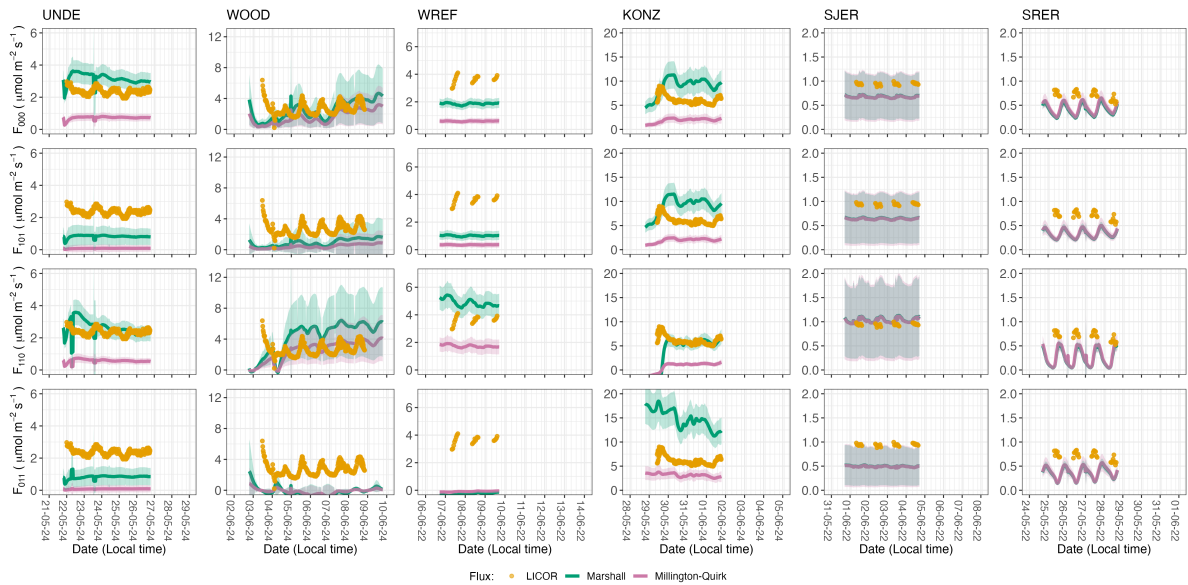


Figure 4: Timeseries of both measured F_S (yellow circles) and modeled soil fluxes (green or purple lines) by the `neonSoilFlux` R package. Fluxes from the `neonSoilFlux` R package are separated by the diffusivity model used (Millington-Quirk or Marshall, Section 4.2.2). Vertical axis labels in the first column represent the measurement levels where the flux-gradient approach is applied (Section 4.2.3). Ribbons for modeled soil fluxes represent ± 1 standard deviation. Results are reported in local time.

294 For a given half-hourly time period, the `neonSoilFlux` packages assigns a QA flag for a mea-

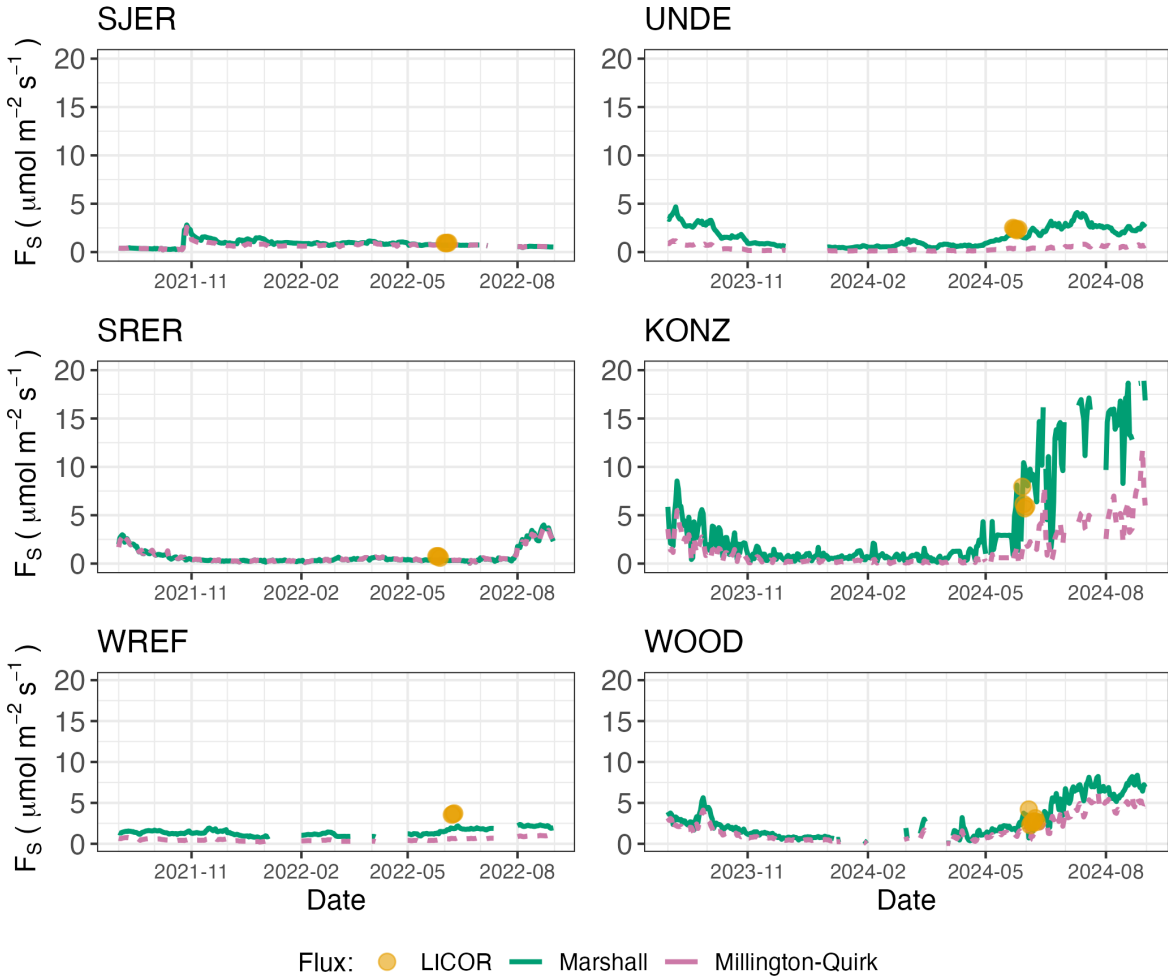
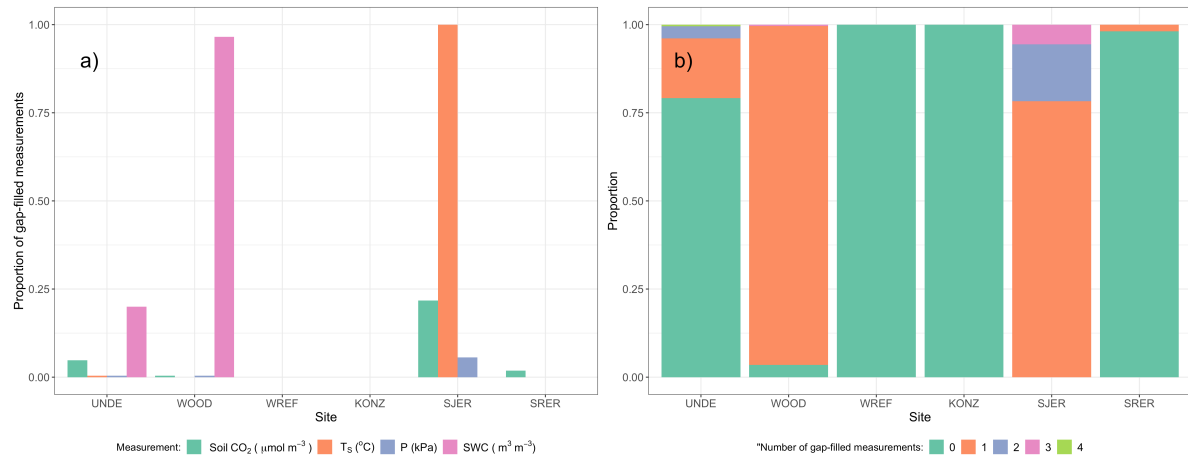


Figure 5: Timeseries of both daily-averaged field F_S (yellow circles) and daily ensemble averaged soil fluxes (green or purple lines) by the `neonSoilFlux` R package, separated by the diffusivity model used (Millington-Quirk or Marshall, Section 4.2.2). The time-series of modeled fluxes are a daily ensemble average of all flux-gradient approaches (F_{000} , F_{101} , F_{011} , F_{110} , Section 4.2.3).

	Millington-Quirk		Marshall	
	NRMSE	R2	NRMSE	R2
KONZ				
F_{110}	0.87	0.41	0.63	0.41
F_{101}	0.69	0.22	0.60	0.15
F_{011}	0.52	0.20	1.35	0.25
F_{000}	0.70	0.23	0.58	0.14
SJER				
F_{110}	0.13	0.17	0.14	0.19
F_{101}	0.32	0.21	0.31	0.24
F_{011}	0.49	0.02	0.48	0.03
F_{000}	0.29	0.18	0.28	0.19
SRER				
F_{110}	0.56	0.00	0.59	0.00
F_{101}	0.66	0.53	0.67	0.52
F_{011}	0.69	0.49	0.70	0.49
F_{000}	0.58	0.51	0.61	0.51
UNDE				
F_{110}	0.76	0.10	0.25	0.02
F_{101}	0.97	0.28	0.66	0.21
F_{011}	0.97	0.15	0.66	0.06
F_{000}	0.70	0.30	0.38	0.05
WOOD				
F_{110}	0.44	0.03	0.93	0.02
F_{101}	0.89	0.07	0.74	0.05
F_{011}	1.12	0.02	1.22	0.01
F_{000}	0.56	0.06	0.46	0.05
WREF				
F_{110}	0.53	0.78	0.35	0.75
F_{101}	0.91	0.24	0.73	0.35
F_{011}	1.03	0.37	1.07	0.37
F_{000}	0.84	0.00	0.49	0.05

Figure 6

295 surement if more one values across all measurement depths uses gap-filled data (Section 4.2.1).
 296 Panel a of Figure 7 reports the distribution for all input environmental measurements at each
 297 site when field measurements were made. Soil fluxes are computed from 4 different types of
 298 input measurements (T_S , SWC , P , and CO_2), any of which could have a QA flag in a half-
 299 hourly interval. Panel b of Figure 7 displays at each site the distribution of the number of
 300 different gap-filled measurements used to compute a half-hourly flux. The largest contribution
 301 to gap-filled measurements was soil water. SJER and WOOD utilized the largest number of
 302 gap-filled measurements, which were primarily SWC and T_S .



303 Figure 7: Panel a) Proportion of input gap-filled environmental measurements used to generate
 304 F_S from the `neonSoilFlux` package, by study site. Panel b) distribution of the usage
 305 of gap-filled measurements at each site.

306 Figure 8 reports both the computed SNR and the proportion of measured field fluxes within the
 307 modeled uncertainty for a given flux computation method F_{ijk} (Section 4.3). Here, values of
 308 SNR greater than unity indicates a reported uncertainty is smaller, propogated by quadrature
 309 from a relatively higher precision from measured input variables (CO_2 , T_S , SWC , or P). The
 310 sensitivity to the uncertainty reduction factor (ϵ , bottom panels in Figure 8) demonstrates
 311 how accuracy could be improved if modeled uncertainty σ_{ijk} decreases.

312 Figure 9 reports the distribution of D_a (from both the Marshall and Millington-Quirk methods,

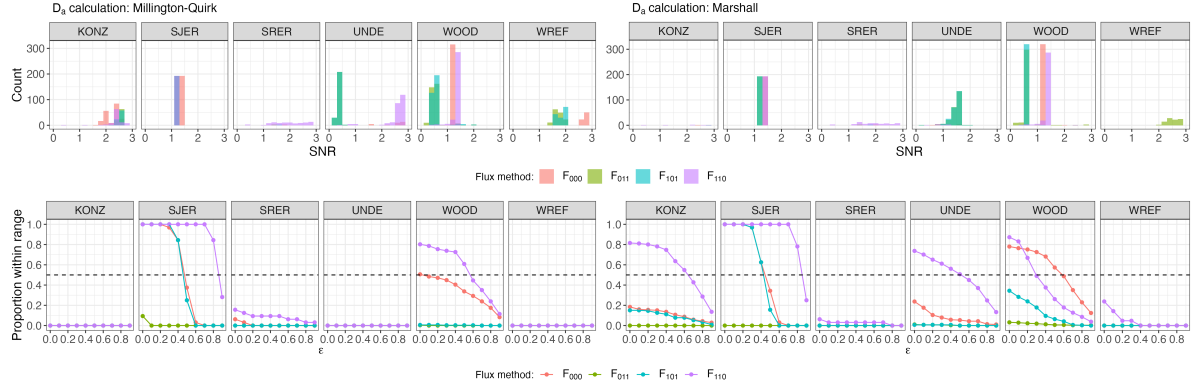


Figure 8: Top panels: distribution of SNR values across each of the different sites for modeled effluxes from the `neonSoilFlux` package, depending on the diffusivity calculation used (Millington-Quirk or Marshall, Section 4.2.2). Bottom panels: Proportion of measured F_S within the modeled range of a flux computation method F_{ijk} given an uncertainty reduction factor ϵ , or $|F_S - F_{ijk}| < (1 - \epsilon)\sigma_{ijk}$.

310 Section 4.2.2) at each study site, and the *post hoc* computation of D_a (Section 4.2.2).

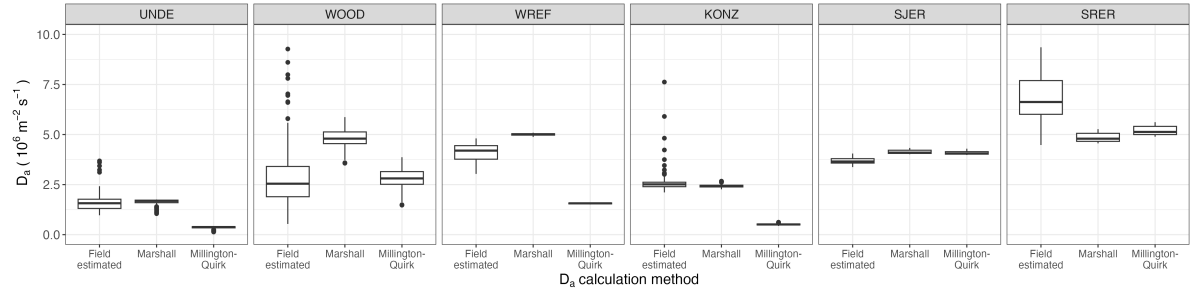


Figure 9

311 6 Discussion

312 This study presents a unified data science workflow to efficiently process automated measure-
 313 ments of belowground soil CO_2 concentrations, water, and temperature to infer estimates of
 314 soil surface CO_2 effluxes through application of Fick's Law (Equation 4). Our core goals in this
 315 study were: (1) to generate estimates of soil flux from continuous soil sensor data at terrestrial

316 NEON sites using the flux-gradient method and then (2) to compare those estimates to field-
317 measured fluxes based on the closed chamber approach at six NEON focal sites. We discuss
318 our progress toward these core goals through (1) an overall evaluation of the flux-gradient ap-
319 proach (and uncertainty calculation) and (2) site-specific evaluation of differences in estimated
320 vs measured fluxes.

321 **6.1 General evaluation of flux-gradient approach**

322 Key assumptions of the flux-gradient approach are that CO₂ concentrations increase through-
323 out the soil profile. We found that this condition was met at XXX% across the study period.
324 Periods where this gradient condition are not met generally are connected to biophysical
325 processes such soil wetting events (e.g. KONZ), which have the effect of reducing the soil res-
326piration or efflux due to a temporary reduction in diffusivity. When modeling soil respiration,
327 typically a non-linear response function that also considers soil type is used (Bouma & Bryla,
328 2000; Yan et al., 2016, 2018). For the `neonSoilFlux` package, soil type is connected to the bulk
329 density, which was characterized at each NEON site based on replicate samples collected from
330 the site megapit at a subset of soil horizons, with an estimated uncertainty of ±5% (see NEON
331 User Guide to Soil physical and chemical properties, Megapit (DP1.00096.001)). Coarse frag-
332 ment estimates also have very large uncertainties, but because the volume fraction tends to
333 be low in surface soils it probably wouldn't contribute much additional flux uncertainty.

334 The largest source of uncertainty to improve reliability of the flux estimate is to prevent the
335 usage of gap-filled data. Three sites (KONZ, SRER, and KONZ) had more than 75% of half-
336 hourly periods with no-gap filled measurements. Two sites (SJER and WOOD) had more
337 than 75% of half-hourly intervals with just one gap-filled measurement. While WREF re-
338 ported no gap-filled measurements, field data collection occurred following a once-in-a century
339 rainstorm with soils observed at their water holding capacity. We recommend that whenever

340 available, local field knowledge is supplementary to any QA filtering protocol of fluxes from
341 the `neonSoilFlux` package.

342 We recognize that this gap-filling approach may lead to gap-filled values that are quite different
343 from the actual values, such as an underestimate of soil moisture following rain events. Further
344 extensions of the gap filling method could use more sophisticated gap-filling routines, similar to
345 what is used for net ecosystem carbon exchange (Falge et al., 2001; Liu et al., 2023; Mariethoz
346 et al., 2015; Moffat et al., 2007; Zhang et al., 2023). The current gap-filling routine provides
347 a consistent approach that can be applied to each data stream, but further work may explore
348 alternative gap-filling approaches.

349 Based on this approach, we would *a priori* expect $F_{011} \leq F_{101} \leq F_{110} \leq F_{000}$ because the
350 previous flux estimates ones correspond to deeper depths which will could miss CO₂ produced
351 in shallower layers. Additionally, field flux measurements should correlate with F_{000} because
352 they represent surface fluxes.

353 **6.2 Evaluation of flux-gradient approach at each site**

354 Derived results from the `neonSoilFlux` package have patterns that are consistent, and
355 comparable, to those directly measured to the field (Figure XXX). The advantage to the
356 `neonSoilFlux` package is the calculation of fluxes across different measurement depths,
357 allowing for additional site-specific customization. Here application of the flux-gradient
358 method provides a baseline estimate of soil fluxes that could be complemented through
359 additional field measurements (e.g. LICOR).

360 The six sites studied provide separate case studies for considerations when applying the flux-
361 gradient method to evaluate resulting uncertainties and fluxes For example, SRER is charac-
362 terized by sandy soil, which also led to the highest observed field soil temperatures. At SRER

363 the flux across the top two layers (F_{110}) produced a pattern of soil flux consistent with the ob-
364 served field data. The remaining methods F_{101} , F_{011} , or F_{000} are derived from information at
365 the deeper layer, which is decoupled both in terms of temperature and CO₂ concentration.

366 In addition, KONZ is a site that experienced a significant rain event prior to sampling with
367 eventual drying out over the course of the experiment. In this case we observed storage of soil
368 water which increased the soil CO₂ at the top layer, leading to negative values of flux at the
369 start of the experiment, with the fluxes drying out afterwards. In this case only when the soil
370 dried out (or returned to a baseline level), that the fluxes at the provided layer would work
371 out in this case.

372 When considering systematic deployment of this method across a measurement network, we
373 faced a number of independent challenges for consideration.

374 Figure 8 illustrates the tradeoff between accuracy for modeled fluxes (defined here as closeness
375 to field-measured F_S) and precision defined by the SNR, and how this is confounded by the
376 choice of diffusivity model used. MORE HERE

377 Diffusivity discussion

378 In developing and validating our approach, we faced a number of challenges related to data
379 availability, including... gap filling, sensor calibration, depth interpolation, rainstorms, etc
380 These errors are all

381 **6.3 Recommendations for future method development**

382 The `neonSoilFlux` package provides three different approaches of values for a soil flux. We
383 believe these approaches reflect a variety of site-specific determination and assumptions used
384 to generate a soil flux measurement (Maier & Schack-Kirchner, 2014), with the choice of

385 method having a determinative approach on reported values. Reported results could further
386 be distilled down using ensemble averaging approaches (Elshall et al., 2018; Raftery
387 et al., 2005).

388 Figures XXX suggests that the provided uncertainty from `neonSoilFlux` is an overestimate
389 compared to what is actually computed. When $\epsilon = 0$ in Figure Figure 8, that means we
390 are just using the reported uncertainty from `neonSoilFlux`. Looking at that ($\text{epsilon} = 0$)
391 shows field measurements UNDE, KONZ, SJER are 100% within the reported intervals from
392 `neonSoilFlux`. But those sites tend to have a $\text{SNR} < 1$, so the uncertainty is pretty noisy. For
393 UNDE, we could even reduce the uncertainty by a factor of 75% ($\text{epsilon} = 0.75$), more than
394 half of the field measurements will still be within the reported intervals. For KONZ, we are
395 still within 70% of the reported intervals when uncertainty is reduced by 90%. That suggests
396 that while the reported accuracy (as compared to field measurements), we do have higher
397 precision.

398 These challenges notwithstanding, the method used here and made available in the
399 `neonSoilFlux` R package has the potential to produce nearly continuous estimates of flux
400 across all terrestrial NEON sites. These estimates are a significant improvement on available
401 approaches to constrain the portion of ecosystem respiration attributable to the soil. This, in
402 turn, aids in our ability to understand the components of net ecosystem flux assessed at these
403 sites using the co-located eddy flux towers.

- 404 • Refine estimates to provide a realistic constraint on surface concentration measurements,
405 thereby increasing the gradient.
- 406 • Apply machine learning algorithms (e.g. random trees) or model averaging techniques to
407 generate a single flux estimate across each sites spatial location
- 408 • Benchmarking flux results to estimates provided by Net ecosystem carbon exchange.

409 **7 Conclusions**

- 410 We have here presented an R package `neonSoilFlux` for the estimation of soil CO₂ fluxes from
411 continuous buried soil sensor measurements across terrestrial National Ecological Observatory
412 Network sites. We compared the predicted fluxes to those measured directly using a field-based
413 closed chamber approach. We find that...
- 414 Baldocchi, D. (2014). Measuring fluxes of trace gases and energy between ecosystems and the
415 atmosphere - the state and future of the eddy covariance method. *Global Change Biology*,
416 20(12), 3600–3609. <https://doi.org/10.1111/gcb.12649>
- 417 Berenbaum, M. R., Carpenter, S. R., Hampton, S. E., Running, S. W., & Stanzione, D. C.
418 (2015). *Report from the NSF BIO Advisory Committee Subcommittee on NEON Scope
419 Impacts*.
- 420 Bond-Lamberty, B. (2018). New Techniques and Data for Understanding the Global Soil Res-
piration Flux. *Earth's Future*, 6(9), 1176–1180. <https://doi.org/10.1029/2018EF000866>
- 421 Bond-Lamberty, B., Ballantyne, A., Berryman, E., Fluet-Chouinard, E., Jian, J., Morris, K.
422 A., Rey, A., & Vargas, R. (2024). Twenty Years of Progress, Challenges, and Opportuni-
423 ties in Measuring and Understanding Soil Respiration. *Journal of Geophysical Research:
424 Biogeosciences*, 129(2), e2023JG007637. <https://doi.org/10.1029/2023JG007637>
- 425 Bond-Lamberty, B., Christianson, D. S., Malhotra, A., Pennington, S. C., Sihi, D., Aghak-
426 ouchak, A., Anjileli, H., Altaf Arain, M., Armesto, J. J., Ashraf, S., Ataka, M., Baldocchi,
427 D., Andrew Black, T., Buchmann, N., Carbone, M. S., Chang, S.-C., Crill, P., Curtis, P.
428 S., Davidson, E. A., ... Zou, J. (2020). COSORE: A community database for continuous
429 soil respiration and other soil-atmosphere greenhouse gas flux data. *Global Change Biology*,
430 26(12), 7268–7283. <https://doi.org/10.1111/gcb.15353>
- 431 Bond-Lamberty, B., & Thomson, A. (2010). A global database of soil respiration data. *Bio-
432 geosciences*, 7(6), 1915–1926. <https://doi.org/10.5194/bg-7-1915-2010>

- 434 Bond-Lamberty, B., Wang, C., & Gower, S. T. (2004). A global relationship between the
435 heterotrophic and autotrophic components of soil respiration? *Global Change Biology*,
436 10(10), 1756–1766. <https://doi.org/10.1111/j.1365-2486.2004.00816.x>
- 437 Bouma, T. J., & Bryla, D. R. (2000). On the assessment of root and soil respiration for soils
438 of different textures: Interactions with soil moisture contents and soil CO₂ concentrations.
439 *Plant and Soil*, 227(1), 215–221. <https://doi.org/10.1023/A:1026502414977>
- 440 Chen, H., & Tian, H.-Q. (2005). Does a General Temperature-Dependent Q10 Model of Soil
441 Respiration Exist at Biome and Global Scale? *Journal of Integrative Plant Biology*, 47(11),
442 1288–1302. <https://doi.org/10.1111/j.1744-7909.2005.00211.x>
- 443 Davidson, E. A., Janssens, I. A., & Luo, Y. (2006). On the variability of respiration in
444 terrestrial ecosystems: Moving beyond Q10. *Global Change Biology*, 12, 154–164. <https://doi.org/10.1111/j.1365-2486.2005.01065.x>
- 445 Desai, A. R., Murphy, B. A., Wiesner, S., Thom, J., Butterworth, B. J., Koupaei-Abyazani, N.,
446 Muttaqin, A., Paleri, S., Talib, A., Turner, J., Mineau, J., Merrelli, A., Stoy, P., & Davis,
447 K. (2022). Drivers of Decadal Carbon Fluxes Across Temperate Ecosystems. *Journal of
448 Geophysical Research: Biogeosciences*, 127(12), e2022JG007014. <https://doi.org/10.1029/2022JG007014>
- 449 450 Elshall, A. S., Ye, M., Pei, Y., Zhang, F., Niu, G.-Y., & Barron-Gafford, G. A. (2018). Relative
451 model score: A scoring rule for evaluating ensemble simulations with application to micro-
452 bial soil respiration modeling. *Stochastic Environmental Research and Risk Assessment*,
453 32(10), 2809–2819. <https://doi.org/10.1007/s00477-018-1592-3>
- 454 Falge, E., Baldocchi, D., Olson, R., Anthoni, P., Aubinet, M., Bernhofer, C., Burba, G.,
455 Ceulemans, R., Clement, R., Dolman, H., Granier, A., Gross, P., Grünwald, T., Hollinger,
456 D., Jensen, N.-O., Katul, G., Keronen, P., Kowalski, A., Lai, C. T., ... Wofsy, S. (2001).
457 Gap filling strategies for defensible annual sums of net ecosystem exchange. *Agricultural
458 and Forest Meteorology*, 107(1), 43–69. [https://doi.org/10.1016/S0168-1923\(00\)00225-2](https://doi.org/10.1016/S0168-1923(00)00225-2)

- 460 Farrance, I., & Frenkel, R. (2012). *Uncertainty of Measurement: A Review of the Rules*
461 *for Calculating Uncertainty Components through Functional Relationships.* *The Clinical*
462 *Biochemist Reviews*, 33(2), 49–75.
- 463 Friedlingstein, P., O’Sullivan, M., Jones, M. W., Andrew, R. M., Bakker, D. C. E., Hauck,
464 J., Landschützer, P., Le Quéré, C., Luijkx, I. T., Peters, G. P., Peters, W., Pongratz, J.,
465 Schwingshackl, C., Sitch, S., Canadell, J. G., Ciais, P., Jackson, R. B., Alin, S. R., Anthoni,
466 P., ... Zheng, B. (2023). Global Carbon Budget 2023. *Earth System Science Data*, 15(12),
467 5301–5369. <https://doi.org/10.5194/essd-15-5301-2023>
- 468 Hamdi, S., Moyano, F., Sall, S., Bernoux, M., & Chevallier, T. (2013). Synthesis analysis
469 of the temperature sensitivity of soil respiration from laboratory studies in relation to
470 incubation methods and soil conditions. *Soil Biology and Biochemistry*, 58, 115–126. <https://doi.org/10.1016/j.soilbio.2012.11.012>
- 472 Hirano, T., Kim, H., & Tanaka, Y. (2003). Long-term half-hourly measurement of soil CO₂
473 concentration and soil respiration in a temperate deciduous forest. *Journal of Geophysical*
474 *Research: Atmospheres*, 108(D20). <https://doi.org/10.1029/2003JD003766>
- 475 Jackson, R. B., Lajtha, K., Crow, S. E., Hugelius, G., Kramer, M. G., & Piñeiro, G. (2017).
476 The Ecology of Soil Carbon: Pools, Vulnerabilities, and Biotic and Abiotic Controls.
477 *Annual Review of Ecology, Evolution and Systematics*, 48(Volume 48, 2017), 419–445.
478 <https://doi.org/10.1146/annurev-ecolsys-112414-054234>
- 479 Jian, J., Bailey, V., Dorheim, K., Konings, A. G., Hao, D., Shiklomanov, A. N., Snyder, A.,
480 Steele, M., Teramoto, M., Vargas, R., & Bond-Lamberty, B. (2022). Historically inconsis-
481 tent productivity and respiration fluxes in the global terrestrial carbon cycle. *Nature*
482 *Communications*, 13(1), 1733. <https://doi.org/10.1038/s41467-022-29391-5>
- 483 Jian, J., Vargas, R., Anderson-Teixeira, K., Stell, E., Herrmann, V., Horn, M., Kholod, N.,
484 Manzon, J., Marchesi, R., Paredes, D., & Bond-Lamberty, B. (2021). A restructured and
485 updated global soil respiration database (SRDB-V5). *Earth System Science Data*, 13(2),

- 486 255–267. <https://doi.org/10.5194/essd-13-255-2021>
- 487 Jiang, J., Feng, L., Hu, J., Liu, H., Zhu, C., Chen, B., & Chen, T. (2024). Global soil
488 respiration predictions with associated uncertainties from different spatio-temporal data
489 subsets. *Ecological Informatics*, 82, 102777. <https://doi.org/10.1016/j.ecoinf.2024.102777>
- 490 Jobbág, E. G., & Jackson, R. B. (2000). The Vertical Distribution of Soil Organic Carbon
491 and its Relation to Climate and Vegetation. *Ecological Applications*, 10(2), 423–436. [https://doi.org/10.1890/1051-0761\(2000\)010%5B0423:TVDOSO%5D2.0.CO;2](https://doi.org/10.1890/1051-0761(2000)010%5B0423:TVDOSO%5D2.0.CO;2)
- 492 Liu, K., Li, X., Wang, S., & Zhang, H. (2023). A robust gap-filling approach for European
493 Space Agency Climate Change Initiative (ESA CCI) soil moisture integrating satellite
494 observations, model-driven knowledge, and spatiotemporal machine learning. *Hydrology
495 and Earth System Sciences*, 27(2), 577–598. <https://doi.org/10.5194/hess-27-577-2023>
- 496 Luo, Y., Ogle, K., Tucker, C., Fei, S., Gao, C., LaDeau, S., Clark, J. S., & Schimel, D. S. (2011).
497 Ecological forecasting and data assimilation in a data-rich era. *Ecological Applications*,
498 21(5), 1429–1442. <https://doi.org/10.1890/09-1275.1>
- 500 Maier, M., & Schack-Kirchner, H. (2014). Using the gradient method to determine soil gas
501 flux: A review. *Agricultural and Forest Meteorology*, 192–193, 78–95. <https://doi.org/10.1016/j.agrformet.2014.03.006>
- 502 Mariethoz, G., Linde, N., Jougnot, D., & Rezaee, H. (2015). Feature-preserving interpolation
503 and filtering of environmental time series. *Environmental Modelling & Software*, 72, 71–76.
504 <https://doi.org/10.1016/j.envsoft.2015.07.001>
- 505 Marshall, T. J. (1959). The Diffusion of Gases Through Porous Media. *Journal of Soil Science*,
506 10(1), 79–82. <https://doi.org/10.1111/j.1365-2389.1959.tb00667.x>
- 507 Millington, R. J., & Shearer, R. C. (1971). Diffusion in aggregated porous media. *Soil Science*,
508 111(6), 372–378.
- 509 Moffat, A. M., Papale, D., Reichstein, M., Hollinger, D. Y., Richardson, A. D., Barr, A. G.,
510 Beckstein, C., Braswell, B. H., Churkina, G., Desai, A. R., Falge, E., Gove, J. H., Heimann,

- 512 M., Hui, D., Jarvis, A. J., Kattge, J., Noormets, A., & Stauch, V. J. (2007). Comprehensive
513 comparison of gap-filling techniques for eddy covariance net carbon fluxes. *Agricultural and*
514 *Forest Meteorology*, 147(3), 209–232. <https://doi.org/10.1016/j.agrformet.2007.08.011>
- 515 Moldrup, P., Olesen, T., Yamaguchi, T., Schjønning, P., & Rolston, D. E. (1999). Modeling
516 diffusion and reaction in soils: 9. The Buckingham-Burdine-Campbell equation for gas
517 diffusivity in undisturbed soil. *Soil Science*, 164(2), 75.
- 518 National Ecological Observatory Network (NEON). (2024a). *Barometric pressure*
519 (*DP1.00004.001*). National Ecological Observatory Network (NEON). <https://doi.org/10.48443/RT4V-KZ04>
- 521 National Ecological Observatory Network (NEON). (2024b). *Soil CO₂ concentration*
522 (*DP1.00095.001*). National Ecological Observatory Network (NEON). <https://doi.org/10.48443/E7GR-6G94>
- 524 National Ecological Observatory Network (NEON). (2024c). *Soil physical and chemical properties*, *Megapit* (*DP1.00096.001*). National Ecological Observatory Network (NEON). <https://doi.org/10.48443/S6ND-Q840>
- 527 National Ecological Observatory Network (NEON). (2024d). *Soil temperature* (*DP1.00041.001*).
528 National Ecological Observatory Network (NEON). <https://doi.org/10.48443/Q24X-PW21>
- 529 National Ecological Observatory Network (NEON). (2024e). *Soil water content and water*
530 *salinity* (*DP1.00094.001*). National Ecological Observatory Network (NEON). <https://doi.org/10.48443/A8VY-Y813>
- 532 Norman, J. M., Kucharik, C. J., Gower, S. T., Baldocchi, D. D., Crill, P. M., Rayment, M.,
533 Savage, K., & Striegl, R. G. (1997). A comparison of six methods for measuring soil-
534 surface carbon dioxide fluxes. *Journal of Geophysical Research: Atmospheres*, 102(D24),
535 28771–28777. <https://doi.org/10.1029/97JD01440>
- 536 Phillips, C. L., Bond-Lamberty, B., Desai, A. R., Lavoie, M., Risk, D., Tang, J., Todd-Brown,
537 K., & Vargas, R. (2017). The value of soil respiration measurements for interpreting and

- 538 modeling terrestrial carbon cycling. *Plant and Soil*, 413(1), 1–25. <https://doi.org/10.1007/s11104-016-3084-x>
- 539
- 540 Raftery, A. E., Gneiting, T., Balabdaoui, F., & Polakowski, M. (2005). *Using Bayesian Model*
541 *Averaging to Calibrate Forecast Ensembles*. <https://doi.org/10.1175/MWR2906.1>
- 542 Sallam, A., Jury, W. A., & Letey, J. (1984). Measurement of Gas Diffusion Coefficient under
543 Relatively Low Air-filled Porosity. *Soil Science Society of America Journal*, 48(1), 3–6.
544 <https://doi.org/10.2136/sssaj1984.03615995004800010001x>
- 545 Shao, J., Zhou, X., Luo, Y., Li, B., Aurela, M., Billesbach, D., Blanken, P. D., Bracho, R.,
546 Chen, J., Fischer, M., Fu, Y., Gu, L., Han, S., He, Y., Kolb, T., Li, Y., Nagy, Z., Niu, S.,
547 Oechel, W. C., ... Zhang, J. (2015). Biotic and climatic controls on interannual variability
548 in carbon fluxes across terrestrial ecosystems. *Agricultural and Forest Meteorology*, 205,
549 11–22. <https://doi.org/10.1016/j.agrformet.2015.02.007>
- 550 Shao, P., Zeng, X., Moore, D. J. P., & Zeng, X. (2013). Soil microbial respiration from
551 observations and Earth System Models. *Environmental Research Letters*, 8(3), 034034.
552 <https://doi.org/10.1088/1748-9326/8/3/034034>
- 553 Sih, D., Gerber, S., Inglett, P. W., & Inglett, K. S. (2016). Comparing models of microbial–
554 substrate interactions and their response to warming. *Biogeosciences*, 13(6), 1733–1752.
555 <https://doi.org/10.5194/bg-13-1733-2016>
- 556 Tang, J., Baldocchi, D. D., Qi, Y., & Xu, L. (2003). Assessing soil CO₂ efflux using continuous
557 measurements of CO₂ profiles in soils with small solid-state sensors. *Agricultural and Forest*
558 *Meteorology*, 118(3), 207–220. [https://doi.org/10.1016/S0168-1923\(03\)00112-6](https://doi.org/10.1016/S0168-1923(03)00112-6)
- 559 Tang, J., Misson, L., Gershenson, A., Cheng, W., & Goldstein, A. H. (2005). Continuous
560 measurements of soil respiration with and without roots in a ponderosa pine plantation
561 in the Sierra Nevada Mountains. *Agricultural and Forest Meteorology*, 132(3), 212–227.
562 <https://doi.org/10.1016/j.agrformet.2005.07.011>
- 563 Taylor, J. R. (2022). *An Introduction to Error Analysis: The Study of Uncertainties in Physical*

- 564 *Measurements, Third Edition* (3rd ed.). University Science Press.
- 565 Yan, Z., Bond-Lamberty, B., Todd-Brown, K. E., Bailey, V. L., Li, S., Liu, C., & Liu, C. (2018).
- 566 A moisture function of soil heterotrophic respiration that incorporates microscale processes.
- 567 *Nature Communications*, 9(1), 2562. <https://doi.org/10.1038/s41467-018-04971-6>
- 568 Yan, Z., Liu, C., Todd-Brown, K. E., Liu, Y., Bond-Lamberty, B., & Bailey, V. L. (2016).
- 569 Pore-scale investigation on the response of heterotrophic respiration to moisture conditions
- 570 in heterogeneous soils. *Biogeochemistry*, 131(1), 121–134. <https://doi.org/10.1007/s10533-016-0270-0>
- 572 Zhang, R., Kim, S., Kim, H., Fang, B., Sharma, A., & Lakshmi, V. (2023). Temporal
- 573 Gap-Filling of 12-Hourly SMAP Soil Moisture Over the CONUS Using Water Balance
- 574 Budgeting. *Water Resources Research*, 59(12), e2023WR034457. <https://doi.org/10.1029/2023WR034457>